Time-Resolved Line Shapes of Single Quantum Emitters via Machine Learned Photon Correlations

Andrew H. Proppe,[1,*] Kin Long Kelvin Lee,[1,2] Alexander E. K. Kaplan,[1] Matthias Ginterseder,[1] Chantalle J. Krajewska,[1] and Moungi G. Bawendi[1,†]

[1]Department of Chemistry, Massachusetts Institute of Technology, Cambridge, Massachusetts 02139, USA
[2]Accelerated Computing Systems and Graphics, Intel Corporation, 2111 25th NE Avenue, Hillsboro, Oregon 97124, USA

(Received 29 January 2023; accepted 26 June 2023; published 4 August 2023)

Solid-state single-photon emitters (SPEs) are quantum light sources that combine atomlike optical properties with solid-state integration and fabrication capabilities. SPEs are hindered by spectral diffusion, where the emitter's surrounding environment induces random energy fluctuations. Timescales of spectral diffusion span nanoseconds to minutes and require probing single emitters to remove ensemble averaging. Photon correlation Fourier spectroscopy (PCFS) can be used to measure time-resolved single emitter line shapes, but is hindered by poor signal-to-noise ratio in the measured correlation functions at early times due to low photon counts. Here, we develop a framework to simulate PCFS correlation functions directly from diffusing spectra that match well with experimental data for single colloidal quantum dots. We use these simulated datasets to train a deep ensemble autoencoder machine learning model that outputs accurate, noiseless, and probabilistic reconstructions of the noisy correlations. Using this model, we obtain reconstructed time-resolved single dot emission line shapes at timescales as low as 10 ns, which are otherwise completely obscured by noise. This enables PCFS to extract optical coherence times on the same timescales as Hong-Ou-Mandel two-photon interference, but with the advantage of providing spectral information in addition to estimates of photon indistinguishability. Our machine learning approach is broadly applicable to different photon correlation spectroscopy techniques and SPE systems, offering an enhanced tool for probing single emitter line shapes on previously inaccessible timescales.

DOI: 10.1103/PhysRevLett.131.053603

Introduction.—Single-photon emitters (SPEs) are the fundamental resource of quantum photonic technologies like quantum communication [1], quantum sensing [2], and quantum computation [3,4]. Solid-state SPEs are particularly attractive systems to achieve this because they combine atomlike optical properties with solid-state fabrication technology and are simple to integrate into cavities. Solid-state SPEs are prone to spectral diffusion, whereby the stochastic environment surrounding the emitter can cause random fluctuations of energy levels [5,6]. For example, in colloidal semiconductor quantum dots (QDs), one well-known mechanism by which this occurs is the quantum-confined Stark effect, where localized charges near the dot surface or in trap states interact with the delocalized exciton states of the QD core [7]. Spectral diffusion is known to be a limiting mechanism of photon indistinguishability in epitaxial QDs [8–11], and also broadens the linewidths of defects in diamonds [12] and 2D materials like hexagonal boron nitride [13,14].

The timescales of the fluctuations that give rise to spectral diffusion can range from subnanoseconds to minutes. Because of limited photon counts from single emitters, the timescale for accumulating enough photons to achieve a sufficiently high signal-to-noise ratio is typically on the order of 100 ms. Below these timescales, photon correlation techniques are typically required, where fast spectral fluctuations can be converted into intensity fluctuations that are resolved with subnanosecond timing using single-photon detectors [8,12].

In a specialized implementation of this technique called photon correlation Fourier spectroscopy (PCFS) [15], the photon stream is passed through an unbalanced Michelson interferometer followed by two single-photon detectors. A schematic of this optical setup is shown in Fig. 1(a). As the path length difference δ between the two interferometer arms is scanned, photon intensity correlation functions $g^{(2)}(\tau,\delta)$ are collected. The photon timing in τ provides temporal resolution, whereas the Fourier transform of scanning the interferometer across δ provides energetic resolution.

In PCFS, $g^{(2)}(\tau,\delta)$ is related to the time-dependent spectrum of the emitter by [15]

$$g^{(2)}(\tau,\delta) = 1 - \frac{1}{2}\cos(2\omega_0 V\tau/c)\mathcal{F}[p(\zeta,\tau)], \qquad (1)$$

where ω_0 is the central frequency of the emitter, V is the scanning frequency of the interferometer retroreflector, c is the speed of light, $\mathcal{F}$ indicates a Fourier transform, and $p(\zeta,\tau)$ is the spectral correlation of the emitter—which is

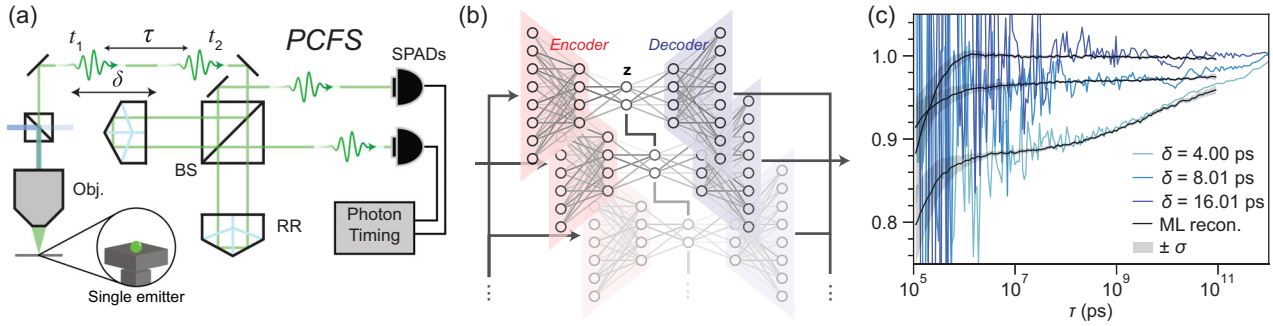

FIG. 1. (a) Schematics of a PCFS setup and (b) architecture of the AAE network. (c) Representative correlation functions with ML reconstructions and standard deviations ($\pm\sigma$).

the autocorrelation of the emission spectrum $s(\omega)$ at time τ. The PCFS $g^{(2)}(\tau,\delta)$ therefore directly encodes time-dependent spectral information of an SPE, with arbitrary temporal and spectral resolution theoretically limited only by total path length δ, the number of stage positions, and the detector timing resolution. In reality, the correlations become extremely noisy at early τ because so few photons are collected in these narrow time bins. A single PCFS experiment can require hours, depending on the number of stage positions used and the brightness of the emitter, making these experiments time-consuming or, worse, impossible for SPEs with limited photostability.

One way to alleviate this signal-to-noise ratio issue is fitting or signal reconstruction. Analytical forms of $g^{(2)}(\tau,\delta)$ for emitters undergoing different types of spectral diffusion exist [15], but they are limited, and require *a priori* assignment of a model to the data, which given high levels of noise and uncertainty will impart bias onto the fit. In contrast, machine learning (ML) approaches can obviate explicit model selection by instead incorporating a variety of models into the training data. ML models have been used to classify quantum emitters based on sparse $g^{(2)}$ data [16], to distinguish light sources with low mean photon numbers [17], and to perform reconstructions in quantum state tomography [18].

Recently, we developed an ML model that could perform signal reconstruction of few-shot pulsed $g^{(2)}(\tau)$ data [19]. By combining several denoising autoencoders in a deep ensemble and employing adversarial training, our adversarial autoencoder ensemble (AAE) model [Fig. 1(b)] could produce probabilistic, denoised reconstructions with similar accuracies and lower variance than maximum likelihood estimation [20] and Levenberg-Marquardt fitting algorithms. Here, we extend our machine learning AAE model to $g^{(2)}(\tau,\delta)$ functions from PCFS experiments of single colloidal QDs [Fig. 1(c)]. All methods and codes for data generation and model training can be found in Ref. [21] [see also Supplemental Material (SM) [22]].

Generating correlations from diffusing spectra.—The connections between spectrum $s(\omega)$, spectral correlation $p(\zeta,\tau)$, interferogram $I(\delta,\tau)$, and finally the correlation functions $g^{(2)}(\tau,\delta)$ are illustrated in Fig. 2. First, we generate $s(\omega)$, in this case a triplet of Lorentzian peaks. For this work, we assumed narrow (μeV) linewidths to simulate SPEs at cryogenic temperatures, but the results are general to all emission line shapes and temperatures.

Next, $s(\omega)$ is convolved with a τ-dependent diffusion process that models the broadening of the peak. For colloidal QDs, the one-dimensional Wiener model is often used:

$$p_d(\zeta,\tau) = \frac{1}{\sqrt{2\pi\alpha^2\tau}}\exp\left(\frac{-\zeta^2}{2\alpha^2\tau}\right), \tag{2}$$

This formula gives a Gaussian whose full width at half maximum (FWHM) increase as $\tau^{0.5}$, where α is the spectral diffusivity coefficient, and determines the timescale over

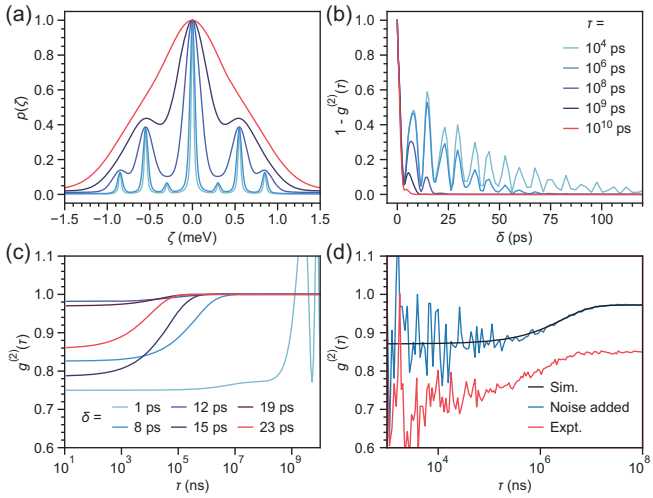

FIG. 2. (a) Simulated homogeneous spectrum $s(\omega)$ of an emitter with three emissive states convolved with a Wiener diffusing Gaussian to form the spectral correlation $p(\zeta,\tau)$. (b) Fourier transform of $p(\zeta,\tau)$ along ζ gives the corresponding interferograms $I(\delta,\tau)$. (c) $g^{(2)}(\tau,\delta)$ functions drawn from $I(\delta,\tau)$. (d) A noiseless simulated $g^{(2)}$ (Sim.) with noise added through Poisson sampling, compared with experimental data (offset for clarity).

which the spectrum is predisposed to diffuse [27]. When $s(\omega)$ is convolved with $p_d(\zeta,\tau)$ to form the total spectral correlation $p(\zeta,\tau)$, absolute energy is lost. The axis ζ is therefore the energy differences between photon pairs. A triplet $s(\omega)$ will lead to a septet in $p(\zeta,\tau)$, as shown in Fig. 2(a).

Fourier transformation of $p(\zeta,\tau)$ along the ζ axis turns energy difference into distance δ and forms the corresponding interferograms $I(\delta,\tau)$ [Fig. 2(b)]. Here, we can observe that $I(\delta,\tau)$ built from longer τ—corresponding to more spectrally diffused and broader $p(\zeta,\tau)$—decay more sharply, due to the lower coherence lengths.

From the full two-dimensional array of $I(\delta,\tau)$, the $g^{(2)}(\tau,\delta)$ functions are then readily calculated using Eq. (1). Examples of $g^{(2)}(\tau,\delta)$ for various values of δ are shown in Fig. 2(c). To probe dynamics across many decades of time, the time bins are made such that they grow exponentially larger with τ, with specified precision (number of bins) and time bounds [28]. To simulate noise, we perform exponentially weighted Poisson sampling at each time bin. Details of this process are given in the SM [22]. The Poisson sampled, simulated correlations show strong resemblance to experimental data [Fig. 2(d)] and are suitable as inputs to train our neural network models.

Modified models for spectral diffusion.—Beyler *et al.* explored continuous versus discrete spectral diffusion mechanisms in CdSe/CdS QDs, showing that whereas continuous diffusion is modeled by a Wiener process for Brownian motion, a spectrum diffusing according to a discrete Gaussian random walk—as is often observed for colloidal dots at 4 K—requires a Poisson model [27]:

$$\mathcal{F}[p(\zeta,\tau)] = \exp\{-r\tau[1-\exp(-2\pi^2\sigma_s^2\delta^2)]\}, \quad (3)$$

where r is the jump kinetic rate constant and σ_s is the linewidth of the diffusing subpopulation. An example of Poisson diffusion using Eq. (3) is shown in Fig. 3(a). When using these models to simulate $g^{(2)}(\tau,\delta)$, it became apparent that regardless of the parameters used, the correlations would always trend to reach 1, and never an intermediate value [Fig. 3(b)]. This originates from the fact that the models allow unlimited broadening of $p(\zeta,\tau)$ with τ. In experimental correlation functions, we observed that correlations could plateau at intermediate values below 1, indicating that spectral diffusion occurs, but does not completely randomize the correlations (see Fig. S2 in SM [22]).

We introduced parameters such that $p(\zeta,\tau)$ could not broaden infinitely, but instead reach a maximum value of σ. We also varied the power of τ in order to control the power law governing the timescale of the diffusion. For the Wiener model, the modified equation takes the form of

$$p_d(\zeta,\tau) = \frac{1}{\sqrt{\pi\xi}}\exp\left(\frac{-\zeta^2}{\left(\frac{\sigma}{1+e^{-\xi}}\right)}\right), \quad \xi = 2\alpha^2\tau^p, \quad (4)$$

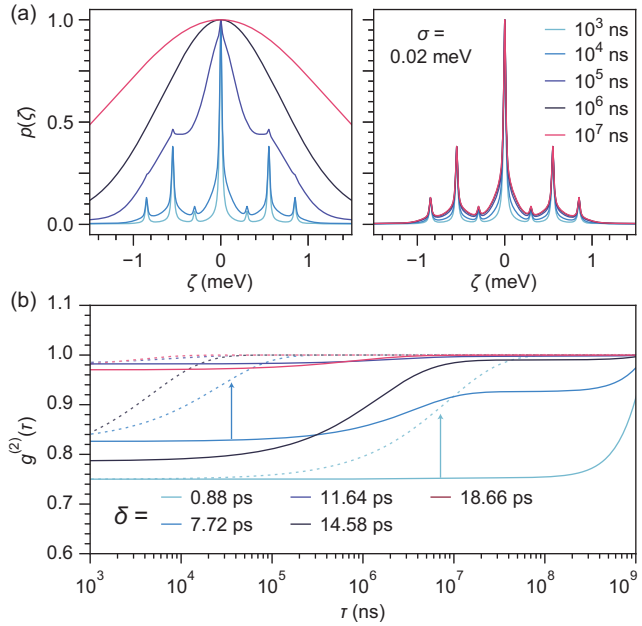

FIG. 3. (a) $p(\zeta,\tau)$ for a triplet undergoing Poisson diffusion without (left) and with (right) a maximum linewidth parameter σ. (b) Simulated $g^{(2)}(\tau,\delta)$ for the Poisson diffusion with [solid lines, Eq. (S6) [22]] and without [dashed lines, Eq. (S5) [22]] the maximum linewidth. Vertical arrows indicate how the correlations are shifted without a limit on σ.

where a sigmoid function in the exponential denominator saturates the linewidth and p controls the power of τ. Similarly, we modify the Poisson model as

$$\mathcal{F}[p(\zeta,\tau)] = \exp\left\{-\sigma/\left[1+\left(\frac{\lambda}{\sigma}\right)^{-1}\right][1-\exp(-2\pi^2\sigma_s^2\delta^2)]\right\}, \quad \lambda = r\tau^p. \quad (5)$$

The resulting $p(\zeta,\tau)$ distributions more closely resemble those we observe experimentally [Fig. 3(a)]. Moreover, the corresponding $g^{(2)}(\tau,\delta)$ can plateau to values below 1, and control of the power law allows for a more gradual increase of the correlations that match experimental observations [Fig. 3(b)]. When comparing $p(\zeta,\tau)$ for the modified and unmodified models with $\sigma \gg \Gamma$, where Γ is the linewidth of peaks in $s(\omega)$, we can observe that both distributions broaden identically, indicating that our modifications have not altered the original physics of the diffusion models (see Figs. S3 and S4 in SM [22]).

Machine learned reconstructions of $g^{(2)}(\tau,\delta)$.—To generate training data, we combined different models of $s(\omega)$ and $p_d(\zeta,\tau)$ to achieve the greatest variance in our simulated correlation functions. For spectra, we used 1–3 Lorentzian peaks, which are often observed for $CsPbBr_3$ perovskite nanocrystals [29,30]. We also used Lorentzian singlets or doublets with acoustic sidebands to simulate

spectra observed in CdSe/CdS or InP/ZnSe quantum dot systems [31,32]. See SM for example spectra [22]. For diffusion models, we used the modified Wiener and Poisson models as described above. Parameters for $s(\omega)$ and $p(\zeta,\tau)$ were randomly selected from within user-defined bounds (Tables S1 and S2 in SM [22]) to generate PCFS interferograms. We simulated 1000 separate PCFS interferograms, each comprising 100 stage positions, for a total of 100 000 $g^{(2)}(\tau,\delta)$ functions. We additionally performed data augmentation, by combining 25 000 random combinations of $g^{(2)}(\tau,\delta)$ from different PCFS experiments, in order to account for systems that may undergo hybrid forms of diffusion (see SM). Poisson sampling of the data was performed during training to help prevent overfitting. An example of a small training dataset of $g^{(2)}(\tau,\delta)$ functions is shown in Fig. S6 [22].

As in our previous work [19], our AAE model is a deep ensemble of denoising autoencoders [33,34]. Previously, we made use of encoders composed of multilayer perceptrons (MLPs, fully connected layers), and an MLP decoder. For these PCFS $g^{(2)}(\tau,\delta)$ functions, adapting the network to have convolutional encoder and decoder layers gave the better accuracy and the smoothest reconstructions. Convolutional layers are significantly more parameter efficient than MLPs, affording a lightweight model with a total of 902 K trainable parameters. Details about model training, loss versus number of epochs, hyperparameters, and a comparison between MLP and convolutional networks are given in the SM (see Figs. S7–S10 [22]).

Predictions from the trained AAE for simulated and experimental $g^{(2)}(\tau,\delta)$ functions are shown in Fig. 4, and several more predictions are provided in Fig. S12 [22]. For experimental data, we collected PCFS correlation functions from single $CsPbBr_3$ quantum dots cooled to 4 K (experimental details given in SM [22]). The model produces smooth, noiseless, and probabilistic outputs across all τ. The model mean prediction (μ) closely follows the true underlying function, and only starts to deviate at early τ where the noise is highest. In nearly all cases, μ is still within $\pm\sigma$, demonstrating the accuracy of the model's reconstructions. As desired, uncertainty scales with τ: at early times with fewer photons per bin, $\pm\sigma$ is larger, while the converse is true for later τ. Predictions for interpolated experimental $g^{(2)}(\tau,\delta)$ functions are shown in Fig. 4(a) (bottom), where the same observations hold true. Clearly, the AAE is able to produce high-fidelity predictions from experimental inputs after being trained solely on our simulated datasets. We can use these reconstructed $g^{(2)}(\tau,\delta)$ functions to build $I(\delta,\tau)$ and Fourier transform into $p(\zeta,\tau)$ to obtain time-dependent line shapes.

Coherence times on nanoscale timescales.—We now have access to a denoised $I(\delta,\tau)$ at early τ. We can reinforce the physicality of the reconstructed $I(\delta,\tau)$ by subsequently fitting it at a given τ. This fitting approach allows for a straightforward estimation of the linewidth $\Gamma(\tau)$, which is related to the optical coherence time $T_2(\tau)$ by the relation $T_2(\tau)=\Gamma(\tau)/2\pi$. For SPEs, maximizing T_2 is crucial to achieving indistinguishable single-photon emission in the transform limit of $T_2=2T_1$, where T_1 is the emitter's radiative lifetime. $CsPbBr_3$ nanocrystals have recently gained intense interest as SPEs due to their exceptionally short T_1 below 200 ps [30] and $T_2(\tau)$ up to 78 ps, with corresponding linewidths of 17 μeV [29]. These values were reported from PCFS experiments with $\tau<100$ μs,

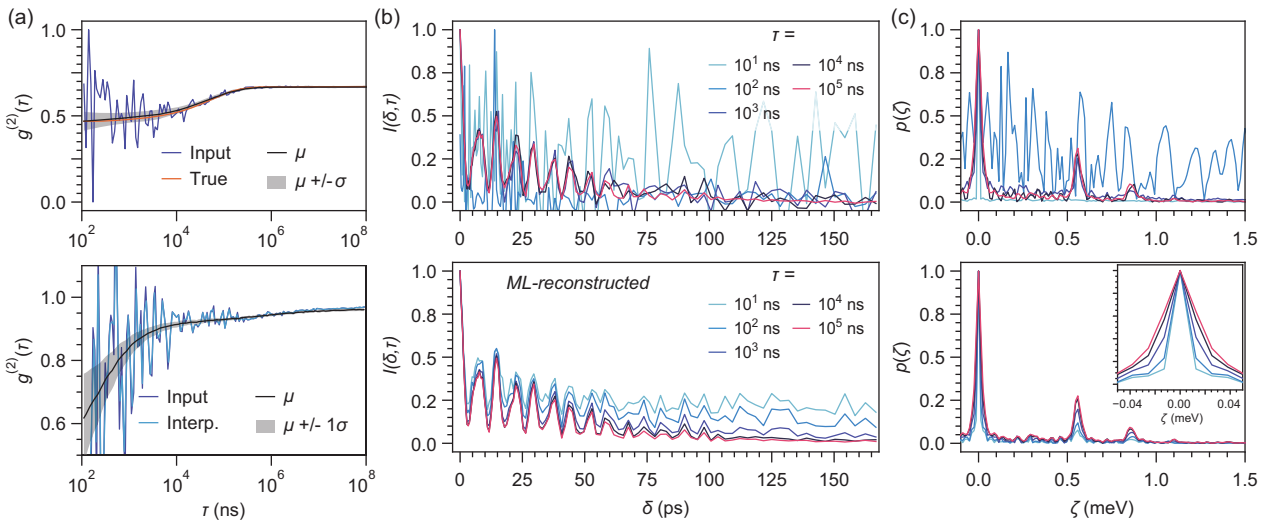

FIG. 4. (a) Top: simulated true and noise-added PCFS $g^{(2)}(\tau,\delta)$ inputs with AAE predicted mean output and standard deviation $\mu\pm\sigma$. Bottom: predictions for afterpulsing-corrected experimental $g^{(2)}(\tau,\delta)$ inputs from a $CsPbBr_3$ quantum dot. Inputs were interpolated to match the input dimension size of the AAE model. (b) $I(\delta,\tau)$ built without (top) and with (bottom) ML-reconstructed $g^{(2)}(\tau,\delta)$. (c) Fourier transformations of $I(\delta,\tau)$ into $p(\zeta)$. Inset in lower panel: enlarged view of the central peak, showing diffusion occurring on timescales down to 10 ns. Uncertainties ($\pm\sigma$) for the ML-reconstructed $I(\delta,\tau)$ are omitted for clarity, and shown in Fig. S14 [22].

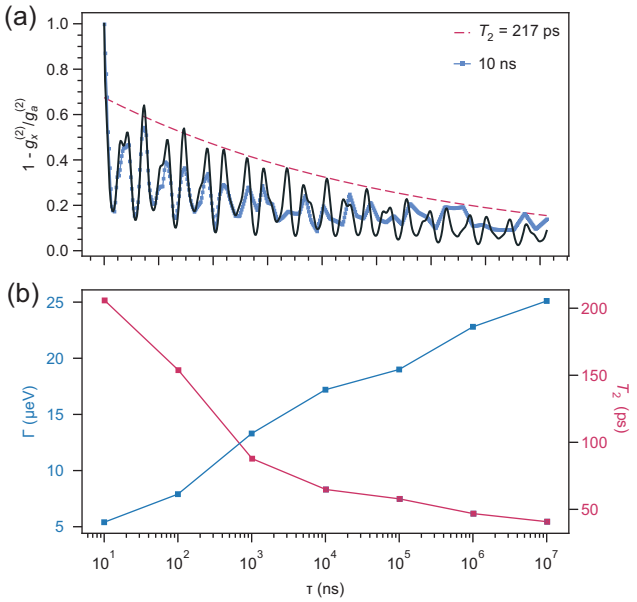

FIG. 5. (a) Fitted experimental, ML-reconstructed $I(\delta,\tau)$ from a $CsPbBr_3$ quantum dot for $\tau = 10$ ns. (b) Extracted linewidths (Γ) and corresponding values of T_2 extracted from fits to $I(\delta,\tau)$ between 10^1 and 10^7 ns.

where $T_2(\tau)$ at earlier τ was inaccessible due to noise. In the context of quantum light generation, nanosecond to few-microsecond timescales are important temporal windows within which to probe spectral diffusion: photons from SPEs are typically generated at megahertz rates, and interference of two consecutively generated photons (i.e., the Hong-Ou-Mandel effect [35,36]) requires them to be indistinguishable, therefore having undergone no spectral diffusion [37].

With the AAE-reconstructed $I(\delta,\tau)$, we can now extract $T_2(\tau)$ on these timescales. A fit of $I(\delta,\tau)$ at $\tau = 10$ ns is shown in Fig. 5(a). Because of the much higher signal-to-noise ratio at later τ, we can reliably fit $I(\delta,\tau)$ on these timescales. We can use these fitted parameters as prior knowledge for fitting at earlier (noisier) τ, assuming only $\Gamma(\tau)$ changes with τ. Fits of the interferogram at $\tau = 10^1 - 10^7$ ns are shown Fig. S14 [22], and a plot of the fitted $\Gamma(\tau)$ and $T_2(\tau)$ versus τ is shown in Fig. 5(c), where we clearly observe $T_2(\tau)$ continues to increase as τ decreases, reaching up to 217 ps for $\tau = 10$ ns. Assuming a T_1 of ~200 ps for this dot, we estimate $T_2/2T_1 = 0.54$ on these timescales. We have recently obtained Hong-Ou-Mandel (HOM) two-photon interference visibilities up to ~0.55 for these same $CsPbBr_3$ nanocrystals [38], which affirms the validity of our modeling. Our AAE reconstructions have allowed us to observe that significant spectral diffusion occurs between 10 ns and 0.1 ms, decreasing $T_2(\tau)$ by more than a factor of 4.

Conclusions.—Our machine learning augmentation to PCFS allows it to access the same nanosecond timescales as HOM correlation functions, but with significant advantages. Firstly, PCFS measures the entire time-resolved lineshape, including phonon sidebands, so there is no need to isolate the zero-phonon line with spectral filtering—the emitter linewidth and coherent fraction are measured directly. Secondly, the emitted photons need not be indistinguishable, since PCFS measures the interference of single photons with themselves, rather than two-photon interference. While most previous work using PCFS investigated spectral diffusion on longer timescales, our advance elevates it to a tool that can be used to study the quantum light-emitting properties of novel solid-state SPEs.

This work furthers our ability to model spectral diffusion in solid-state SPEs and offers a pipeline for converting these models into simulated, noise-added $g^{(2)}(\tau,\delta)$ functions to train denoising neural network models. Photon correlation spectroscopy is among the most powerful and flexible tools for characterizing solid-state SPEs. With the deep learning model developed herein, probing nanosecond timescales is now possible in PCFS experiments and can be used to characterize solid-state SPEs toward realizing quantum photonic technologies.

A. H. P., A. E. K. K., M. G., and C. J. K. were supported by the U.S. Department of Energy, Office of Science, Basic Energy Sciences under Award No. DE-SC0021650. A. H. P. was additionally supported by a Postdoctoral Fellowship from the Natural Sciences and Engineering Research Council of Canada (NSERC). K. L. K. L. was supported by Intel Corporation. A. H. P. developed simulations, designed neural network models and performed training, acquired experimental data, and performed all analyses. A. E. K. K. assisted with acquiring experimental data. M. G. and C. J. K. were responsible for synthesis of $CsPbBr_3$ perovskite quantum dots and C. J. K. was responsible for synthesis of $CsPbBr_3$ perovskite quantum dots. K. L. K. L. designed the original denoising adversarial autoencoder ensemble neural network models. M. G. B. supervised the project. All authors read and commented on the manuscript.

*Current address: Joint Center for Extreme Photonics, National Research Council of Canada and University of Ottawa, 100 Sussex Drive, Ottawa, Ontario, K1A 0R6, Canada.
†Corresponding author.
mgb@mit.edu

[1] X. Lu *et al.*, Chip-integrated visible–telecom entangled photon pair source for quantum communication, Nat. Phys. **15**, 4 (2019).
[2] X. Guo *et al.*, Distributed quantum sensing in a continuous-variable entangled network, Nat. Phys. **16**, 281 (2020).
[3] E. Knill *et al.*, A scheme for efficient quantum computation with linear optics, Nature (London) **409**, 6816 (2001).
[4] L. S. Madsen *et al.*, Quantum computational advantage with a programmable photonic processor, Nature (London) **606**, 7912 (2022).

[5] M. J. Fernée *et al.*, Spontaneous spectral diffusion in CdSe quantum dots, J. Phys. Chem. Lett. **3**, 1716 (2012).
[6] S. A. Empedocles *et al.*, Influence of spectral diffusion on the line shapes of single CdSe nanocrystallite quantum dots, J. Phys. Chem. B **103**, 1826 (1999).
[7] S. A. Empedocles *et al.*, Quantum-confined Stark effect in single CdSe nanocrystallite quantum dots, Science **278**, 2114 (1997).
[8] K. Gao *et al.*, Nanosecond-scale spectral diffusion in the single photon emission of a GaN quantum dot, AIP Adv. **7**, 125216 (2017).
[9] Y.-M. He *et al.*, On-demand semiconductor single-photon source with near-unity indistinguishability, Nat. Nanotechnol. **8**, 213 (2013).
[10] M. Khoshnegar *et al.*, A solid state source of photon triplets based on quantum dot molecules, Nat. Commun. **8**, 15716 (2017).
[11] D. Dalacu *et al.*, Nanowire-based sources of non-classical light, Nanotechnology **30**, 232001 (2019).
[12] J. Wolters, N. Sadzak, A. W. Schell, T. Schroder, and O. Benson, Measurement of the Ultrafast Spectral Diffusion of the Optical Transition of Nitrogen Vacancy Centers in Nano-Size Diamond Using Correlation Interferometry, Phys. Rev. Lett. **110**, 027401 (2013).
[13] B. Spokoyny *et al.*, Effect of spectral diffusion on the coherence properties of a single quantum emitter in hexagonal boron nitride, J. Phys. Chem. Lett. **11**, 1330 (2020).
[14] S. White *et al.*, Phonon dephasing and spectral diffusion of quantum emitters in hexagonal boron nitride, Optica **8**, 1153 (2021).
[15] X. Brokmann *et al.*, Photon-correlation Fourier spectroscopy, Opt. Express **14**, 6333 (2006).
[16] Z. A. Kudyshev *et al.*, Rapid classification of quantum sources enabled by machine learning, Adv. Quantum Technol. **3**, 2000067 (2020).
[17] C. You *et al.*, Identification of light sources using machine learning, Appl. Phys. Rev. **7**, 021404 (2020).
[18] S. Ahmed, C. Sánchez Muñoz, F. Nori, and A. F. Kockum, Quantum State Tomography with Conditional Generative Adversarial Networks, Phys. Rev. Lett. **127**, 140502 (2021).
[19] A. H. Proppe *et al.*, Adversarial autoencoder ensemble for fast and probabilistic reconstructions of few-shot photon correlation functions for solid-state quantum emitters, Phys. Rev. B **106**, 045425 (2022).
[20] C. L. Cortes, S. Adhikari, X. Ma, and S. K. Gray, Accelerating quantum optics experiments with statistical learning, Appl. Phys. Lett. **116**, 184003 (2020).
[21] github reference, https://github.com/andrewhproppe/g2-pcfs-ML.
[22] See Supplemental Material at http://link.aps.org/supplemental/10.1103/PhysRevLett.131.053603 for description of supplemental material: materials & methods, details of simulations and dataset creation, and supplemental figures and tables, which includes Refs. [23–26].
[23] A. Paszke *et al.*, PyTorch: An imperative style, high-performance deep learning library, in *Advances in Neural Information Processing Systems 32*, edited by H. Wallach, H. Larochelle, A. Beygelzimer, F. d'Alché-Buc, E. Fox, and R. Garnett (Curran Associates, Inc., Red Hook, New York, 2019), pp. 8024–8035.
[24] W. Falcon *et al.*, PyTorchLightning/PyTorch-Lightning: 0.7.6 Release (2020), https://github.com/Lightning-AI/lightning.
[25] D. P. Kingma *et al.*, ADAM: A method for stochastic optimization, arXiv:1412.6980.
[26] Weights & Biases–Developer Tools for ML, https://wandb.ai/site.
[27] A. P. Beyler, L. F. Marshall, J. Cui, X. Brokmann, and M. G. Bawendi, Direct Observation of Rapid Discrete Spectral Dynamics in Single Colloidal CdSe-CdS Core-Shell Quantum Dots, Phys. Rev. Lett. **111**, 177401 (2013).
[28] T. A. Laurence, S. Fore, and T. Huser, Fast, flexible algorithm for calculating photon correlations, Opt. Lett. **31**, 829 (2006).
[29] H. Utzat *et al.*, Coherent single-photon emission from colloidal lead halide perovskite quantum dots, Science **363**, 1068 (2019).
[30] M. A. Becker *et al.*, Bright triplet excitons in caesium lead halide perovskites, Nature (London) **553**, 7687 (2018).
[31] L. Besombes, K. Kheng, L. Marsal, and H. Mariette, Acoustic phonon broadening mechanism in single quantum dot emission, Phys. Rev. B **63**, 155307 (2001).
[32] A. Brodu *et al.*, Exciton fine structure and lattice dynamics in InP/ZnSe core/shell quantum dots, ACS Photonics **5**, 3353 (2018).
[33] D. P. Kingma *et al.*, An introduction to variational autoencoders, Found. Trends® Mach. Learn. **12**, 307 (2019).
[34] P. Baldi, Autoencoders, unsupervised learning, and deep architectures, in *Proceedings of ICML Workshop on Unsupervised and Transfer Learning*, edited by I. Guyon, G. Dror, V. Lemaire, G. Taylor, and D. Silver (PMLR, Bellevue, Washington, USA, 2012), pp. 37–49.
[35] F. Bouchard *et al.*, Two-photon interference: The Hong-Ou-Mandel effect, Rep. Prog. Phys. **84**, 012402 (2020).
[36] A. M. Brańczyk, Hong-Ou-Mandel interference, arXiv:1711.00080.
[37] A. Thoma *et al.*, Exploring Dephasing of a Solid-State Quantum Emitter via Time- and Temperature-Dependent Hong-Ou-Mandel Experiments, Phys. Rev. Lett. **116**, 033601 (2016).
[38] A. E. K. Kaplan *et al.*, Hong-Ou-Mandel interference in colloidal $CsPbBr_3$ perovskite nanocrystals, Nat. Photonics (2023).